nature nanotechnology

Article

https://doi.org/10.1038/s41565-023-01383-6

Hierarchically resistive skins as specific and multimetric on-throat wearable biosensors

Received: 5 December 2021

Accepted: 22 March 2023

Published online: 27 April 2023

Check for updates

Shu Gong[1,6], Xin Zhang[2,3,6], Xuan Anh Nguyen[4], Qianqian Shi[1], Fenge Lin[1], Sunita Chauhan[4], Zongyuan Ge[2,3,5] ✉ & Wenlong Cheng[1] ✉

Resistive skin biosensors refer to a class of imperceptible wearable devices for health monitoring and human–machine interfacing, in which conductive materials are deposited onto or incorporated into an elastomeric polymeric sheet. A wide range of resistive skins has been developed so far to detect a wide variety of biometric signals including blood pressure, skin strain, body temperature and acoustic vibrations; however, they are typically non-specific, with one resistive signal corresponding to a single type of biometric data (one-mode sensors). Here we show a hierarchically resistive skin sensor made of a laminated cracked platinum film, vertically aligned gold nanowires and a percolated gold nanowire film, all integrated into a single sensor. As a result, hierarchically resistive skin displays a staircase-shaped resistive response to tensile strain, with distinct sensing regimes associated to a specific active material. We show that we can, through one resistive signal, identify up to five physical or physiological activities associated with the human throat speech: heartbeats, breathing, touch and neck movement (that is, a multimodal sensor). We develop a frequency/amplitude-based neural network, Deep Hybrid-Spectro, that can automatically disentangle multiple biometrics from a single resistive signal. This system can classify 11 activities—with different combinations of speech, neck movement and touch—with an accuracy of 92.73 ± 0.82% while simultaneously measuring respiration and heart rates. We validated the classification accuracy of several biometrics with an overall accuracy of >82%, demonstrating the generality of our concept.

Biological worlds are naturally intelligent systems, whereas electronics are artificially intelligent systems. The two types of systems are distinct and incompatible. Emerging soft electronics have the potential to serve as second-skin-like wearable patches[1–3] for monitoring human health vitals[4,5], designing perception robotics[6] and bridging interactions between natural and artificial intelligence (NI–AI)[7]. Human throat skin is unique in that it is related to multiple biometrics such as speech, heart and respiration rates, neck movement and tactile finger touch; however, a convergent NI–AI system cannot be realized with traditional sensors that are bulky and rigid, and incompliant to throat skin[8]. The emerging skin-like wearable piezoelectric[9], capacitive[10], triboelectric[11,12] and resistive[13] sensors can potentially overcome

[1]Department of Chemical and Biological Engineering, Monash University, Melbourne, Australia. [2]Department of Electrical and Computer Systems Engineering, Monash University, Melbourne, Australia. [3]Monash Medical AI, Monash University, Melbourne, Australia. [4]Department of Mechanical and Aerospace Engineering, Monash University, Melbourne, Australia. [5]Monash-Airdoc Research Center, Monash University, Melbourne, Australia. [6]These authors contributed equally: Shu Gong, Xin Zhang. ✉e-mail: zongyuan.ge@monash.edu; wenlong.cheng@monash.edu

https://doi.org/10.1038/s41565-023-01383-6

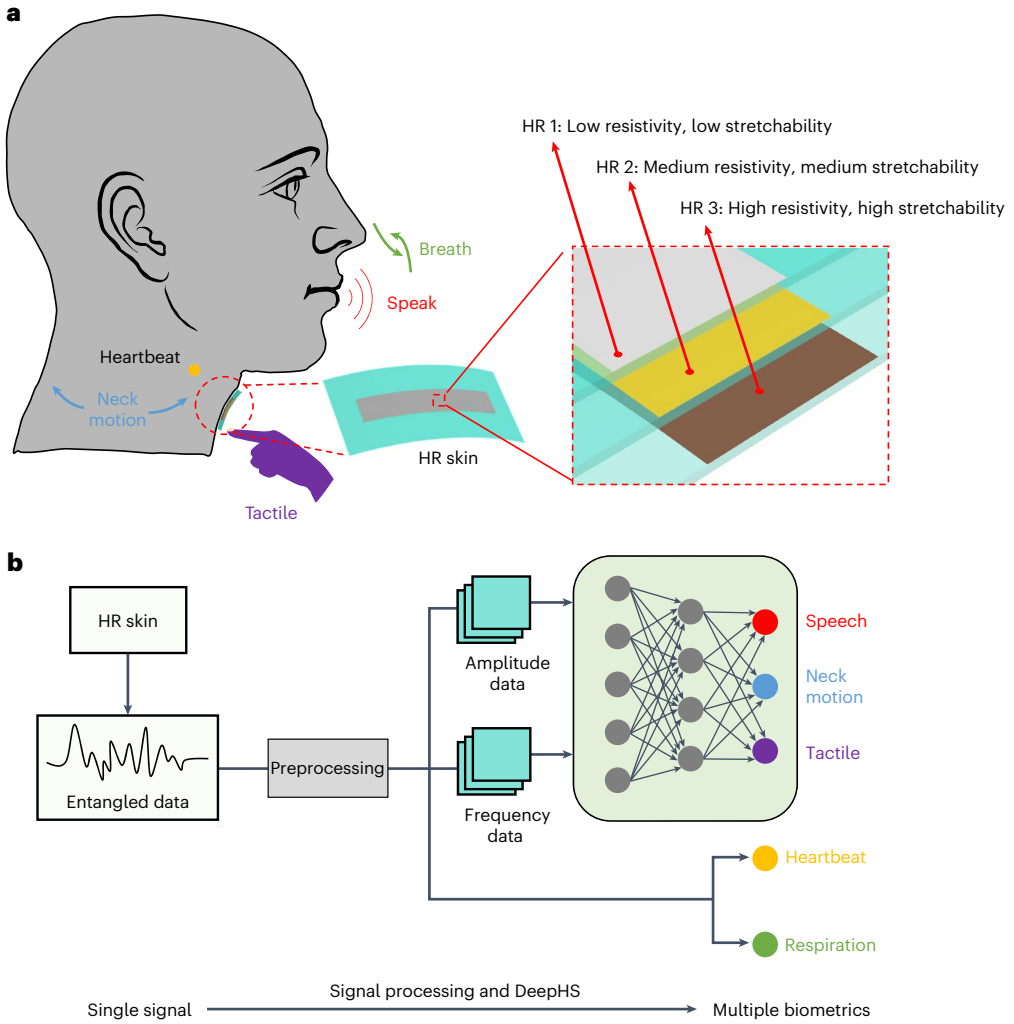

Fig. 1 | Bio-inspired HR-skin-neuron network sensory processing framework. **a**, Schematic of the wearable HR skin as a single biosensor to report multiple biometrics including physical (speech, neck motion and tactile) and physiological (respiration and heart rates) information. **b**, Framework of our HR skin sensory system to disentangle a single resistive signal into multiple classified biometrics via our data process and DeepHS.

this challenge. In particular, resistive skins can combine ultrathinness with facile device integration, and hence offer a simple yet efficient approach to fabricate electronic skins[14] and tattoos[2,15,16] for detecting various biometric signals such as pressure[17], strain[18], temperature[16] and acoustic vibration[19].

Despite encouraging advances, the current soft electronic sensors are still largely non-specific and single-modal—mismatching the human skin sensory system, which is multimodal and highly specific[20]. Although multiple types of wearable sensing patches/tattoos may be used, they are impractical given the enormous pixels required to seamlessly connect naturally and artificially intelligent systems.

Here we report on a hierarchically resistive (HR) skin that can overcome the aforementioned challenges—offering the ability to disentangle a single resistive signal into multiple types of biometric data. This HR skin was devised to have three resistive skin layers with unique resistivity and stretchability, but sharing common leads to minimize the number of pixels required (Fig. 1a), which could be realized with low-resistivity cracked platinum film, medium-resistivity vertically aligned gold nanowires (v-AuNWs) and high-resistivity ultrathin gold nanowires (u-AuNWs). Such fabricated HR skins exhibited distinct staircase-shaped electrical responses and linearity in three different strain ranges, leading to identification of five physical/psychological activities (speech, heart and respiration rates, touch and neck movement) when worn on the throat. The single resistive data could be disentangled and classified into 11 specific real-world activities with an overall accuracy of 92.73 ± 0.82% by our multimodal Deep Hybrid-Spectro (DeepHS)—a custom signal processing and convolutional neural network (CNN) framework (Fig. 1b). We believe that the HR skin concept offers a promising solution to establish convergent NI–AI systems for broad applications in future remote healthcare, soft robotics and human–machine interactions.

Design principles

Figure 2a illustrates an example of a wearable on-throat HR skin sensor, which is composed of cracked platinum film, v-AuNWs and u-AuNWs sandwiched from top to bottom sequentially with polydimethylsiloxane (PDMS) layers in between. The overall device was flexible with a thickness of ~118 μm (Fig. 2b,c). The respective internal structures of the active layers were confirmed via transmission electron microscopy characterizations of microtomed samples (Fig. 2d–f). In a typical HR skin sensor, platinum, v-AuNWs and u-AuNWs had sheet resistances of 25.2 ± 6.4 Ω sq^{-1}, 4.9 ± 1.7 kΩ sq^{-1} (refs. 16,19) and 2.0 ± 0.9 MΩ sq^{-1} (ref. 21), respectively (Supplementary Fig. 1).

Our proposed HR design concept requires not only a staircase-like resistance profile, but also distinct sensitivity for each active layer, namely, high conductivity and high sensitivity for the top layer; medium conductivity and medium sensitivity for the middle layer; and low conductivity and low sensitivity for the bottom layer. To

https://doi.org/10.1038/s41565-023-01383-6

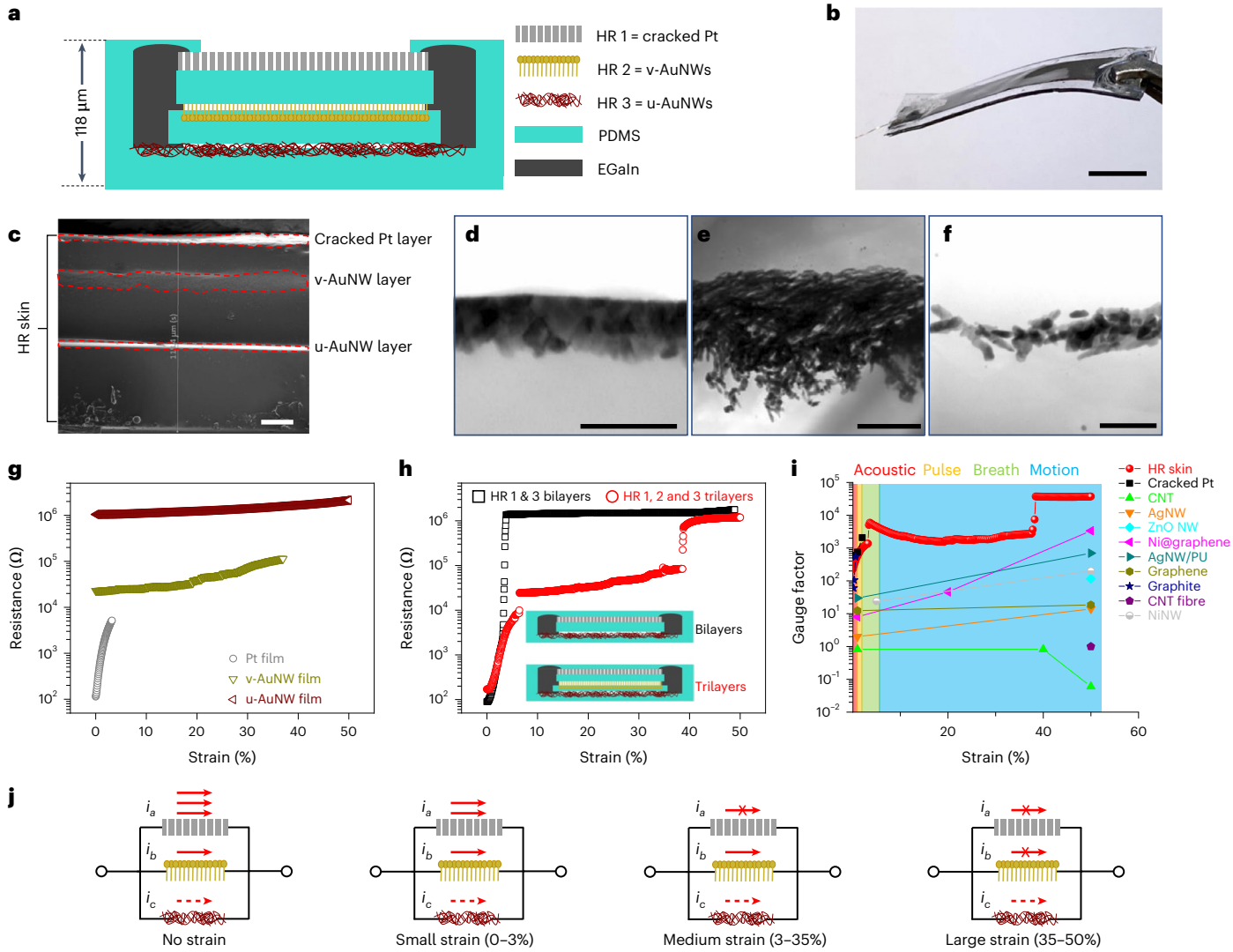

Fig. 2 | Structure design, characterization and working principles of the HR skin. a, Schematic illustration of the structure of the HR skin. EGaIn refers to Eutectic gallium-indium. **b**, Photograph of the HR skin. Scale bar, 2 mm. **c**, Cross-sectional scanning electron microscope (SEM) image of the HR skin. Scale bar, 20 µm. **d**–**f**, Transmission electron microscopy images of the cross-sectional view of cracked platinum (top layer, **d**), v-AuNWs (middle layer, **e**) and u-AuNWs (bottom layer, **f**). Scale bars, 50 nm (**d**), 200 nm (**e**) and 50 nm (**f**). **g**, The resistance changes of each individual layer in the 0–50% strain range. **h**, The resistance changes of HR skin comprising bilayers of cracked platinum film/u-AuNWs, and trilayers of cracked platinum film/v-AuNWs/u-AuNWs, in the 0–50% strain range. **i**, Comparison of dynamic gauge factors between HR skin and other resistive electronic skins in the literature[13,18,22–29]. CNT refers to carbon nanotube. **j**, The sensing mechanism of the trilayer HR skin. i_a, i_b and i_c are defined as the current passing through the top, middle and bottom layers, respectively, when a constant voltage is applied.

achieve this, we carefully investigated the conductivity, sensitivity and stretchability of each layer by fine tuning their respective thicknesses (Supplementary Figs. 2–4). We found that 20 nm cracked platinum exhibited the highest sensitivity of the thicknesses between 20 and 60 nm (Supplementary Fig. 2b). As for the v-AuNWs, films with a growth time of 1 min showed distinct conductivity compared with cracked platinum (Supplementary Fig. 3a). Finally, double-layer u-AuNWs were chosen due to their stable and distinct conductivity compared with v-AuNWs (Supplementary Fig. 4a). Thus, 20 nm cracked platinum (Supplementary Fig. 5), 1-min-growth-time v-AuNWs (Supplementary Fig. 6) and double-layer self-assembled thin film u-AuNWs (Supplementary Fig. 7) were chosen for the design of the HR skin sensor, with resistances of 10^2–10^4 Ω, 10^4–10^5 Ω and 10^6–10^7 Ω, within 0–50% strain, respectively (Fig. 2g).

With this design, the HR skin conductor displayed staircase-shaped resistance changes to tensile strains, with high linearity in the specific small (ε = 0–3%), medium (ε = 3–35%) and high (ε = 35–50%) strain regimes (Fig. 2h, open red circles). As a result, our HR skin maintained an ultrahigh gauge factor of >10^2 with respect to a full strain range of 0.01–50% (Fig. 2i, filled red spheres), which has not been achieved by a single resistive sensor in the literature[13,18,22–29]. The high sensitivity and specificity of our HR skin enable identification of specific signals associated with different types of throat activities including vocal cords vibration, carotid artery pulsing, respiration and neck movement.

The working principle of the HR skin is illustrated in Fig. 2j. When a constant voltage is applied to the sensing circuit, the majority of the redox current would pass through the low-resistivity top platinum layer when a small tensile strain (ε = 0–3%) is applied. At medium strain (3–35%), the top platinum layer will be electrically non-conductive, thereby activating the medium-resistivity v-AuNW layer. Further increasing the strain to >35% will block electron transport in both the top and middle layers, in which the high-resistivity u-AuNW layer dominates the overall current.

Specific responses to acoustic forces, pressure and strains

Compared with the literature[9–13,30–32], we found that our wearable on-throat HR skin displayed high specificity, and could therefore identify specific pressure, tensile strain and acoustic vibration. To demonstrate this, a pressing probe, an actuating moving stage and a speaker were located at the top, side and bottom of the suspended HR skin, respectively (Fig. 3a). The device exhibited stable and periodic electrical output across a 50–1,000 Hz frequency range, showing a rapidly reducing trend before 200 Hz followed by a gradually decreasing trend with little fluctuation in the range of 200–1,000 Hz (Fig. 3b). The acoustic sensitivity can be calculated using equation (1):

$$S = \frac{(R - R_0)/R_0}{P_0 \times 10^{L_p/20}} \quad (1)$$

where R and R_0 are the resistances of the sensor before and after acoustic vibration, respectively, P is the reference sound pressure of 2×10^{-5} Pa, and L_p is the sound pressure level in decibels. The acoustic sensitivity of the device reached 0.33 Pa^{-1} at a constant frequency of 200 Hz and specific distance of 1 mm with the sound source (Fig. 3c), which gradually decreased with an increase in the speaker–sensor distance. Note that acoustic vibration only triggered small resistive changes, indicating the top platinum layer dominates.

By contrast, we found that the middle v-AuNW layer governed the specific resistive responses to the tensile strain in the 5–35% range (Fig. 3d), displaying high linearity with an averaged gauge factor of 2,111.2 (Fig. 3e). The cyclic resistance changes under a stretching frequency of 0.25 Hz were stable and uniform at various strains (Fig. 3f). Furthermore, the resistance amplitude was independent of the stretching frequencies (Supplementary Fig. 8). With the specific strains of 0.02% and 0.8% applied, fast response times of 9 and 12 ms were achieved, respectively (Supplementary Fig. 9).

Next, pressure in the 10–100 kPa range was applied to our HR skin in the vertical direction, mimicking skin touch force from gentle to forceful (Fig. 3g). We found a much more substantial resistive response (Fig. 3h), indicating the dominant role of the bottom u-AuNW layer. A high sensitivity of 106.6 kPa^{-1} was achieved with an excellent signal-to-noise ratio (SNR) in response to specific dynamic pressures (Fig. 3i).

We further applied tensile and acoustic loads simultaneously (Fig. 3j), which activated both the top platinum and middle v-AuNW layers. We compared the resistive response with dynamic strain only, and with strain plus acoustic vibration. The profiles in both conditions were almost the same (Fig. 3k), indicating that the tensile strain signal is not affected by the additional acoustic vibration stimuli. Nevertheless, FFT analysis revealed an input frequency of 200 Hz (Fig. 3l), which was absent for the strain-only sample. We note the acoustic signal faded for strains >4% (inset of Fig. 3k), possibly due to the electrical failure of the cracked platinum layer. Similarly, our HR skin could also pick up tiny acoustic and large pressure signals simultaneously (Fig. 3m–o).

Durability and throat activities recognition

Our HR skin displayed durable staircase-shaped electrical responses to various strain levels (Supplementary Fig. 10). There was a negligible deterioration in signal quality even after 500 continuous stretch–release cycles. The HR skin also responded steadily and reversibly, with large strains of up to 50% for more than 1,000 continuous cycles (Supplementary Fig. 11), proving that the electrical failure of the top and middle layers did not affect the electrical durability of the device. This agrees with our structural characterizations: the individual active layers of the HR skin displayed reversible morphological recovery following 50% strain release (Supplementary Fig. 12). The laminated active materials were very thin, which did not alter the mechanical properties of PDMS (Supplementary Fig. 13). The plasma treated surfaces offered strong interfacial bonding forces against delamination even at 50% strain (Supplementary Fig. 14). Furthermore, the HR skin, as a well encapsulated and skin-compatible device, was also chemically stable. Negligible performance degradation was recorded, even after being soaked in the artificial perspiration and undergoing 1,000 continuous stretch–release cycles (Supplementary Fig. 15).

We further applied our HR skin to specifically detect a variety of throat-related activities (Fig. 4a,b). Initially, the male volunteer breathed normally under the static conditions. The large respiration peaks and small pulse peaks were clearly identified with averaged peak amplitudes of 0.18 ± 0.05 and 0.012 ± 0.003, respectively (Fig. 4c). Afterwards, the volunteer started to speak. Remarkably, the speaking regions could be accurately identified simply via short-time Fourier transform (STFT) analysis (Fig. 4b). We could clearly see the individual acoustic vibration peaks overlaid on top of the large respiration and pulse peaks (Fig. 4d) with a distinct voice/no-voice boundary area (Fig. 4e). Note that high-frequency acoustic signals were not detected by a single u-AuNW layer due to its low sensitivity at low levels of strain (0–3%) (Supplementary Fig. 16). Finally, three neck stretching movements were applied, leading to substantial, ~1,000-fold resistance changes—equivalent to a tensile strain of >35% (Fig. 4b). This activated the u-AuNW layer and deactivated both the top platinum and middle v-AuNW layers.

We further compared the HR skin with individual platinum, v-AuNW and u-AuNW sensors in response to carotid artery pulsing, breathing, speech, neck movement and touch (Fig. 4f). Evidently, the cracked platinum sensor dominated in the small strain range ($0\% < \varepsilon < 3\%$)—exhibiting similar resistance changes and SNR levels to our HR skin—but failed to detect neck movement and touch due to its limited stretchability. The v-AuNWs could detect the neck flexion, but not for carotid artery pulsing, breathing and speaking. The u-AuNWs sensor responded stably to neck movement and finger touch, but failed to detect small strains induced by speech, breathing and pulsing. By contrast, only the HR skin showed reliable responses towards all five throat-related activities with distinct amplitude and SNR (Fig. 4f).

Moreover, the HR skin showed distinct signal patterns in response to deep, normal and mild breaths (Supplementary Fig. 17). As for the neck movements, shaking the head in the horizontal direction would result in large sensor resistance changes in the order of 10^1–10^2, falling into the sensitivity range of the middle v-AuNW layer (Supplementary Fig. 18). Nodding of the head exhibited a >10-times-smaller peak amplitude (Supplementary Fig. 18), falling in the strain range of the top platinum layer. This observation might have originated from the vertically aligned cracks of the platinum film, leading to suppressed sensitivity in response to strains in vertical direction and enhanced sensitivity with strains in horizontal direction[16].

Classification model

Our task involves real-world collected signals with artefacts, for which a standard off-the-shelf machine learning framework would fail easily. The existing algorithms[33–35] are not able to simultaneously solve the problem of rate detection and activity classification, and cannot navigate our diverse signal changes. We therefore developed the custom signal processing and CNN framework, DeepHS, to classify various throat activities, taking advantage of the amplitude characteristic of the raw signal and the pixel relations of its two-dimension spectrogram. For dection of the heart and respiration rates, a bandpass filter was applied to the entangled data for rejecting the irrelevant frequencies (Fig. 5a). As shown in Supplementary Fig. 19, the bandpass filters of the heart and respiration rates were set in the 0.5–3 Hz and 0.1–0.5 Hz, ranges, respectively, after validating the accuracy of our calculation using a reference device. This is consistent with the filter range used in the literature[36]. The heart and breathing rates can be calculated by peaks number under adaptive thresholds (Supplementary Section 4a) over its time duration (Supplementary Fig. 20). We further checked its robustness performance in different situations by adding spoken noises and neck motions both separately and

https://doi.org/10.1038/s41565-023-01383-6

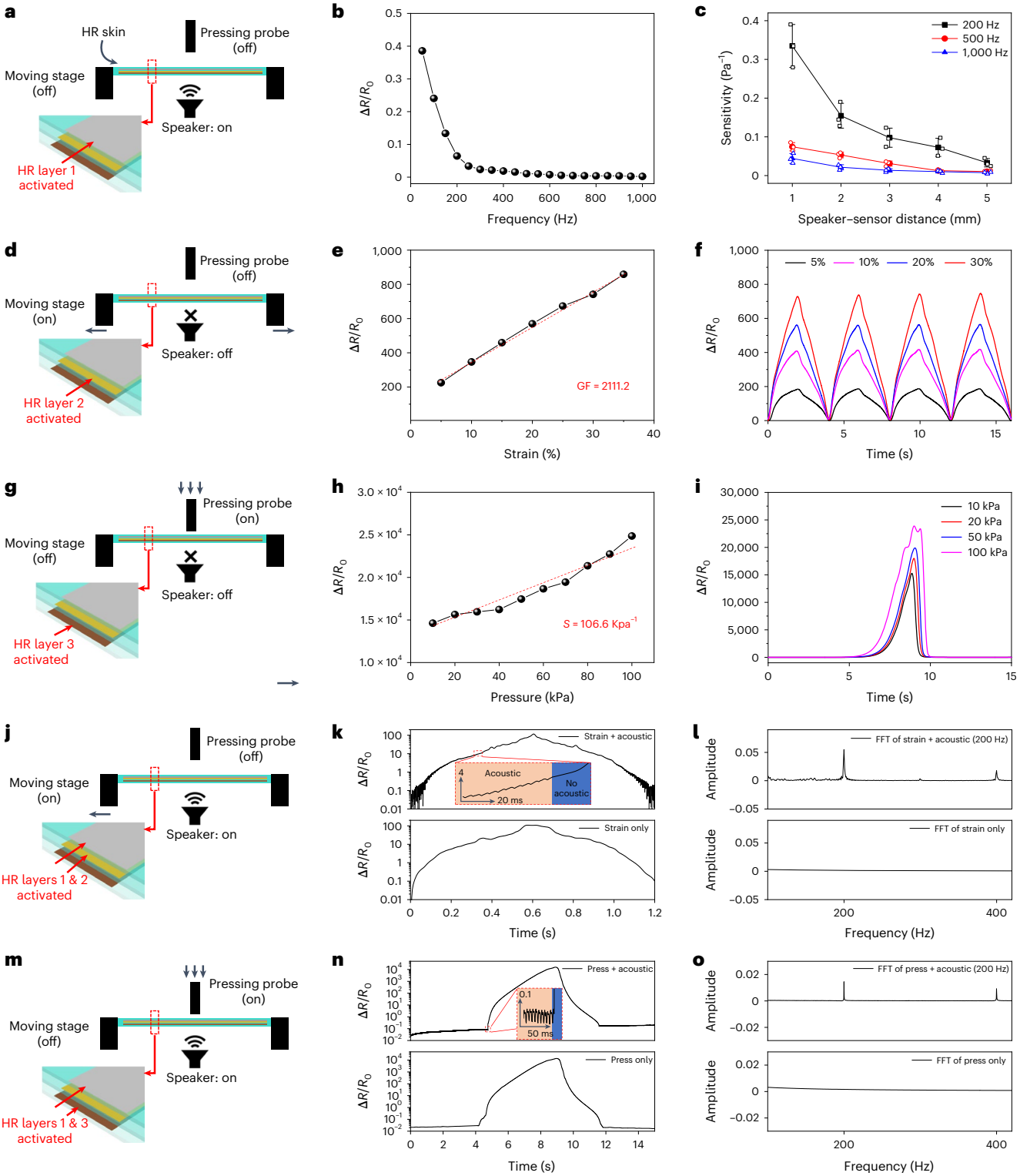

Fig. 3 | Mechano-electrical performance characterization of the HR skin under acoustic, strain and pressure stimulations. a, Schematic illustration of experimental set-up when the HR skin is under acoustic stimulation. **b**, Resistance changes of the HR skin under acoustic stimulation in the human vocal range (100–1,000 Hz). **c**, Acoustic sensitivity of the HR skin with different sound source distances (1–5 mm) at constant sound frequencies of 200, 500 and 1,000 Hz, respectively. The error bars refer to the standard deviation on the basis of three samples ($n = 3$). **d**–**f**, Schematic illustration (**d**), resistance changes (**e**) and dynamic cyclic performance (**f**) of the HR skin when it is under mechanical tensile strain in the range of human skin deformation (5–35%). **g**–**i**, Schematic illustration (**g**), resistance changes (**h**) and dynamic performance (**i**) of the HR skin when it is under mechanical compression in the range of gentle (10 kPa) to forceful (100 kPa) human touch. **j**, Schematic illustration of experimental set-up when the HR skin is under both acoustic and tensile strain stimulation. **k**,**l**, Comparison of dynamic performance (**k**) and fast Fourier transform (FFT) analysis (**l**) of HR skin with (top) and without (bottom) acoustic stimulation (200 Hz) when it is under 0–5% tensile strain. **m**, Schematic illustration of experimental set-up when the HR skin is under both acoustic and compressive pressure stimulation. **n**,**o**, Comparison of dynamic performance (**n**) and FFT analysis (**o**) of HR skin with (top) and without (bottom) acoustic stimulation (200 Hz) when it is under compressive pressure of 10 kPa. Data are presented as mean values ± s.d.

https://doi.org/10.1038/s41565-023-01383-6

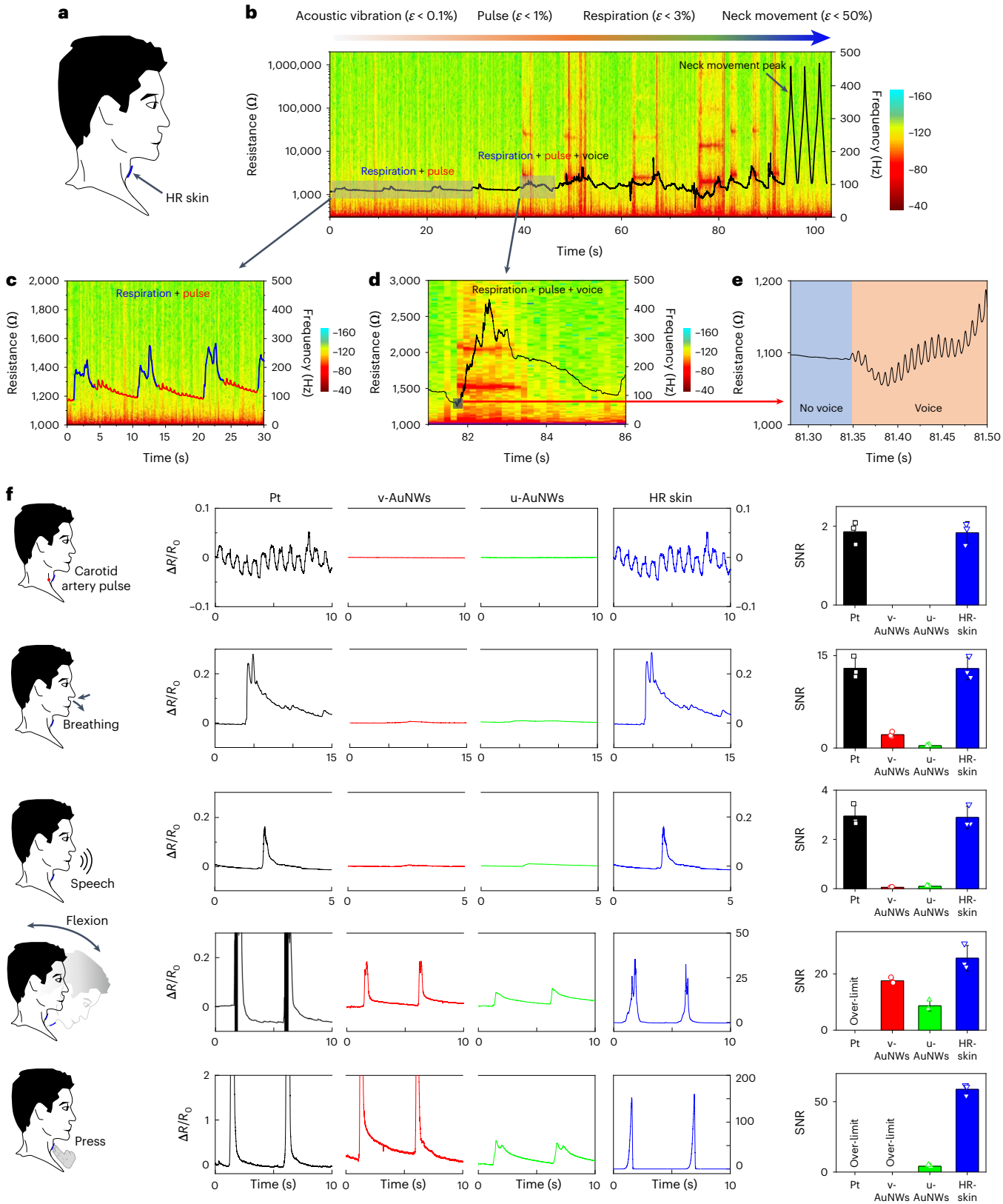

Fig. 4 | Performance evaluation to monitor multilevel throat activities. **a**, Schematic of the HR skin attached on human throat. **b**, The resistance changes (curve) and the STFT analysis (background) of the hierarchical electronic skin in response to normal breathing only (0–40 s), normal breathing and speech (40–92 s), and neck movement (92–103 s). **c**, The enlarged view of the first 30 s to demonstrate the combination of respiration (blue) and pulse (red) peaks, no high-frequency signal is detected in the STFT analysis. **d**, The enlarged view of 81–85 s to demonstrate the combination of respiration and acoustic vibration peaks. The background STFT analysis demonstrates that a high-frequency speech signal is detected at 82–83 s. **e**, The enlarged view of the boundary area before and after speaking. **f**, The resistance changes and their corresponding SNR of each layer and the HR skin under different activities including carotid artery pulsing, breathing, speech, neck movement and finger touch. The error bars refer to the s.d. of the SNR on the basis of three samples ($n = 3$). Data are presented as mean values ± s.d.

https://doi.org/10.1038/s41565-023-01383-6

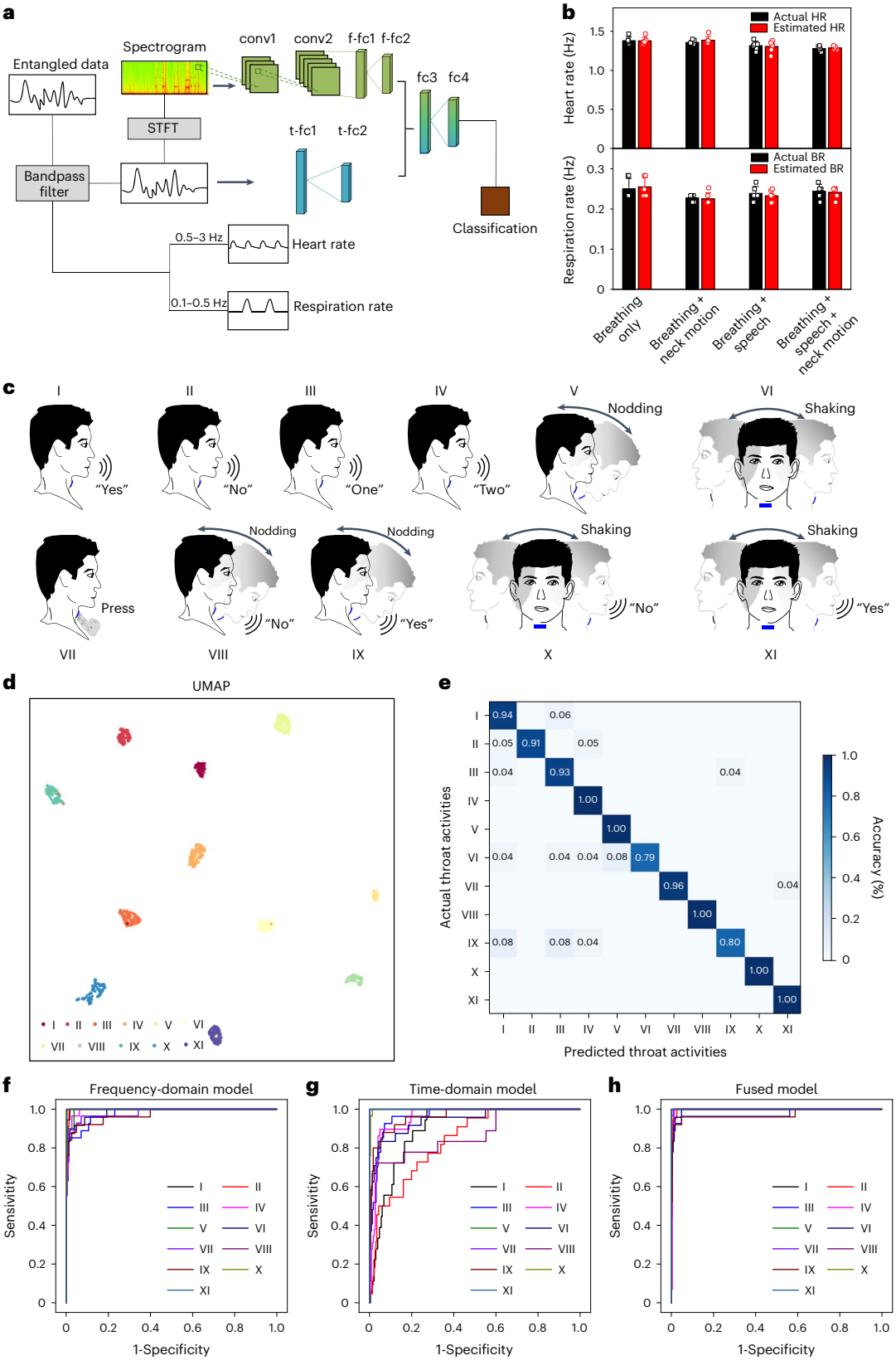

Fig. 5 | Development of DeepHS for classification and recognition of throat activities. a, Schematic of the entangled data processing, heart and respiration rate detections, and the associated deep learning architecture. The phase-dropped spectrogram is extracted from the 1,000 Hz waveform using STFT with an FFT size of 512, a Hann window length of 512 and a hop length of 256. fc, fully connected neural network; conv, convolutional layer. **b**, Testing results of heart and respiration rate detections in different situations compared with the actual rates. The error bars refer to the s.d. of the heart and respiration rates on the basis of six samples ($n = 6$). **c**, Visualization of 11 throat activities. **d**, Visualizing the 1,094 samples of all throat activities by using the UMAP dimension reduction technique. **e**, Testing accuracies of neck motions, speech, touch and combinations of them all. **f**–**h**, Receiver operating characteristic curves of the deep learning-based recognition based on SFTF (**f**), time-series (**g**) and fused (**h**) models. Data are presented as mean values ± s.d.

simultaneously (Supplementary Figs. 21–23). We found that the estimated rates would be affected by these artefacts, as respiration and heart rate peaks would be covered by spoken noises and neck motions; however, the algorithm can be further improved by excluding the speech/motion time before calculation (Supplementary Figs. 21–23 and Fig. 5b).

Regarding the DeepHS shown in Fig. 5a, we initially trained one four-layer multilayer perceptron (MLP) and one CNN for classification using raw signals and STFT spectrograms, respectively. In the time-domain MLP, a batch normalization layer and a leaky rectified linear unit layer were applied sequentially after each linear layer (t-fc1–t-fc2) to make the training process faster and more stable[37], and also to avoid the zero gradient issue[38]. In the frequency-domain CNN, two convolutional layers (conv1–conv2) and two fully connected layers (f-fc1–f-fc2) are followed by a leaky rectified linear unit layer; additional dropout layers with a 30% dropout value of neurons were added after these two fully connected layers to alleviate the potential issue of overfitting. Next, based on two pretrained networks, we trained the third MLP part (fc3–fc4), taking the input of concatenated outputs from the second to last layers from these two networks.

For acquiring our baseline model, the training and testing samples were randomly selected on the basis of a 8:2 ratio from the baseline dataset. Fivefold cross-validation was used to estimate its performance. See Supplementary Section 4b for more information on hyperparameters optimization.

Data collection and performance metrics

We collected a custom dataset comprising 11 classes of spoken words, neck motions, touch, and their combinations, including: saying the words "one"/"two"/"yes"/"no"; nodding or shaking of the head; finger touch; and combinations of nodding of the head with "yes"/"no", and shaking of the head with "yes"/"no" (Fig. 5c). The dataset comprised 1,263 samples, and each sample was composed of the raw signal data of 3 s captured from the HR skin sensor and its corresponding STFT. Due to the invariance of voltage across the HR skin sensor, the continuous current signal was used for classification. Further details on data preprocessing can be found in the 'Data processing' section in the Methods.

For visualizing the distribution of the baseline dataset, we used a potent dimension reduction technique named uniform manifold approximation and projection (UMAP)[39] (Fig. 5d), which projected every 3 s signal to a two-dimension point. These points were grouped as different clusters based on their similarities. All 11 classes of spoken words, touch and/or neck motions are presented. Sensors attached to different neck positions during the collecting process resulted in some samples having a slightly high frequency and time biases. Hence mild overlap inevitably existed in some classes based on UMAP. Overall, the information from both the amplitude and frequency responses captured by HR skin could still furnish the details of different throat activities despite this minor flaw.

We evaluated the performance of our classification model by plotting the receiver operating characteristic curve at different discriminative thresholds (Fig. 5f–h). It plots two parameters called the true positive rate and false positive rate for each threshold, often referred to as sensitivity and 1-specificity, respectively. It was clear that the receiver operating characteristic of the fused model performs better than the other two single models.

According to the experiments, the classification accuracies of the time- and frequency-domain models (Supplementary Fig. 24) could reach up to 76.28% (±1.25%) and 89.57% (±2.26%), respectively. The final classification accuracy of the fused model could reach up to 92.73% (±0.82%) (Fig. 5e). Note that we have performed all kinds of activities with different forces and rates, including gentle/forceful pressing and quick/slow nodding/shaking in our dataset (Supplementary Fig. 25). The classification accuracy of pressing, nodding and shaking is very high (100%, 96%, 79%) despite of a wide variety of actions, indicating high specification of our HR skin and high robustness of DeepHS.

We further evaluated the robustness of DeepHS by testing different subjects. First, we collected a custom baseline dataset from one male and one female for generalization between genders. We also developed a motion artefact-suppressed, suspended layout for data collection (Supplementary Fig. 26). The final classification accuracy of this gender-balanced dataset could reach up to 82.68% (±1.44%) (Supplementary Fig. 27). This pretrained model was further fine-tuned by five participants (three male and two female), whose dataset (ten for each class) was abided by the ratio of 3:2:5 for the training, validation and testing sets. The classification accuracy could reach 84.21% (±5.82%) (Supplementary Fig. 28).

We also evaluated the performance when our HR skin was attached 2 cm above and below the optimized position (Supplementary Fig. 29). Our artificial intelligence-powered HR skin still maintained a high accuracy at 86.0% and 80.7%, in comparison to 92.3% for the optimized position, indicating excellent generality and adaptivity of the hierarchical design and machine learning algorithm despite of misplacement. This satisfactory performance is also the reason why we decided to take advantage of the knowledge from both time and frequency domains for the classification tasks. The efficient DeepHS not only closely fits the data complexity with a short inference time, but also acquire excellent personalization when the fine-tuning datum is very few.

Visualization

As a proof of concept for potential applications, we demonstrated the use of our proposed sensor in apple-picking and robotic-assisted surgery scenarios (Supplementary Videos 1 and 2). A human acted as a master and a robot acted as a servant. Commands from the human were recorded by our wearable sensors and transferred to a DeepHS and the virtual environment through TCP/IP protocol. The human could make commands by voice or movement. The humanoid robot receives a command recognized by DeepHS and reacted accordingly to assist its master. The heart rates of the human could also be monitored simultaneously for telehealth purposes.

Conclusion

Human skin receptors are specific yet multimetric. It remains highly challenging to realize such capability with artificial electronic sensors, in spite of encouraging progress in the burgeoning field of soft bioelectronics. In this Article we have devised a resistive electronic skin conductor by laminating—from top to bottom—cracked platinum film, v-AuNWs and u-AuNWs sequentially, with PDMS layers sandwiched between the active layers. Due to the unique HR properties of each active layer, the HR skin displayed staircase-like electrical profiles in response to tensile strains, which could be used to detect multiplex mechanical stimuli such as normal pressure, tensile strain and acoustic vibration. Despite being a single resistive signal, our HR skin could identify specific human throat activities related to vital health signals (heart and respiration rates), vocal cords vibration and neck movement. We further developed a machine learning algorithm, which was able to disentangle single resistive signals and accurately classify 11 activity combinations from speech, neck movement and their combinations, and successfully recognizing several basic human behaviours such as nodding of the head or saying "yes", and shaking of the head or saying "no". We believe that our HR skin offers a promising strategy to fabricate imperceptive wearable biosensor to bridge natural and artificial intelligence for remote healthcare and seamless human–machine interaction.

Online content

Any methods, additional references, Nature Portfolio reporting summaries, source data, extended data, supplementary information, acknowledgements, peer review information; details of author contributions and competing interests; and statements of data and code availability are available at https://doi.org/10.1038/s41565-023-01383-6.

References

1. Kim, D.-H. et al. Epidermal electronics. *Science* **333**, 838–843 (2011).
2. Miyamoto, A. et al. Inflammation-free, gas-permeable, lightweight, stretchable on-skin electronics with nanomeshes. *Nat. Nanotechnol.* **12**, 907–913 (2017).
3. Wang, S. et al. Skin electronics from scalable fabrication of an intrinsically stretchable transistor array. *Nature* **555**, 83–88 (2018).
4. Yang, Y. et al. A laser-engraved wearable sensor for sensitive detection of uric acid and tyrosine in sweat. *Nat. Biotechnol.* **38**, 217–224 (2020).
5. Sempionatto, J. R. et al. An epidermal patch for the simultaneous monitoring of haemodynamic and metabolic biomarkers. *Nat. Biomed. Eng.* **5**, 737–748 (2021).
6. Shih, B. et al. Electronic skins and machine learning for intelligent soft robots. *Sci. Robot.* **5**, eaaz9239 (2020).
7. Zhou, Z. et al. Sign-to-speech translation using machine-learning-assisted stretchable sensor arrays. *Nat. Electron.* **3**, 571–578 (2020).
8. Hammock, M. L., Chortos, A., Tee, B. C. K., Tok, J. B. H. & Bao, Z. 25th Anniversary article: the evolution of electronic skin (e-skin): a brief history, design considerations, and recent progress. *Adv. Mater.* **25**, 5997–6038 (2013).
9. Dagdeviren, C. et al. Conformable amplified lead zirconate titanate sensors with enhanced piezoelectric response for cutaneous pressure monitoring. *Nat. Commun.* **5**, 4496 (2014).
10. Lee, S. et al. An ultrathin conformable vibration-responsive electronic skin for quantitative vocal recognition. *Nat. Commun.* **10**, 2468 (2019).
11. Yang, J. et al. Eardrum-inspired active sensors for self-powered cardiovascular system characterization and throat-attached anti-interference voice recognition. *Adv. Mater.* **27**, 1316–1326 (2015).
12. Kang, S. et al. Transparent and conductive nanomembranes with orthogonal silver nanowire arrays for skin-attachable loudspeakers and microphones. *Sci. Adv.* **4**, eaas8772 (2018).
13. Kang, D. et al. Ultrasensitive mechanical crack-based sensor inspired by the spider sensory system. *Nature* **516**, 222–226 (2014).
14. Jason, N. N., Ho, M. D. & Cheng, W. Resistive electronic skin. *J. Mater. Chem. C.* **5**, 5845–5866 (2017).
15. Kabiri Ameri, S. et al. Graphene electronic tattoo sensors. *ACS Nano* **11**, 7634–7641 (2017).
16. Gong, S. et al. Local crack-programmed gold nanowire electronic skin tattoos for In-plane multisensor integration. *Adv. Mater.* **31**, 1903789 (2019).
17. Gong, S. et al. A wearable and highly sensitive pressure sensor with ultrathin gold nanowires. *Nat. Commun.* **5**, 3132 (2014).
18. Yamada, T. et al. A stretchable carbon nanotube strain sensor for human-motion detection. *Nat. Nanotechnol.* **6**, 296–301 (2011).
19. Gong, S. et al. A soft resistive acoustic sensor based on suspended standing nanowire membranes with point crack design. *Adv. Funct. Mater.* **30**, 1910717 (2020).
20. Amjadi, M., Kyung, K. U., Park, I. & Sitti, M. Stretchable, skin-mountable, and wearable strain sensors and their potential applications: a review. *Adv. Funct. Mater.* **26**, 1678–1698 (2016).
21. Gong, S. et al. Highly stretchy black gold e-skin nanopatches as highly sensitive wearable biomedical sensors. *Adv. Electron. Mater.* **1**, 1400063 (2015).
22. Amjadi, M., Pichitpajongkit, A., Lee, S., Ryu, S. & Park, I. Highly stretchable and sensitive strain sensor based on silver nanowire–elastomer nanocomposite. *ACS Nano* **8**, 5154 (2014).
23. Xu, X. et al. High-strain sensors based on ZnO nanowire/polystyrene hybridized flexible films. *Adv. Mater.* **23**, 5440 (2011).
24. Han, F. et al. *J. Mater. Chem. C.* **5**, 10167 (2017).
25. Cao, Z., Wang, R., He, T., Xu, F. & Sun, J. Interface-controlled conductive fibers for wearable strain sensors and stretchable conducting wires. *ACS Appl. Mater. Interfaces* **10**, 14087 (2018).
26. Ma, J. et al. Highly sensitive and large-range strain sensor with a self-compensated two-order structure for human motion detection. *ACS Appl. Mater. Interfaces* **11**, 8527 (2019).
27. Liao, X. et al. Flexible and highly sensitive strain sensors fabricated by pencil drawn for wearable monitor. *Adv. Funct. Mater.* **25**, 2395 (2015).
28. Tang, Z. et al. Highly stretchable core–sheath fibers via wet-spinning for wearable strain sensors. *ACS Appl. Mater. Interfaces* **10**, 6624 (2018).
29. Wang, S. et al. Controllable synthesis of nickel nanowires and its application in high sensitivity, stretchable strain sensor for body motion sensing. *J. Mater. Chem. C.* **6**, 4737 (2018).
30. Tao, L.-Q. et al. An intelligent artificial throat with sound-sensing ability based on laser induced graphene. *Nat. Commun.* **8**, 14579 (2017).
31. Wei, Y. et al. A wearable skinlike ultra-sensitive artificial graphene throat. *ACS Nano* **13**, 8639–8647 (2019).
32. Nayeem, M. O. G. et al. All-nanofiber–based, ultrasensitive, gas-permeable mechanoacoustic sensors for continuous long-term heart monitoring. *Proc. Natl Acad. Sci. USA* **117**, 7063–7070 (2020).
33. Zhang, Q., Zeng, X., Hu, W. & Zhou, D. A machine learning-empowered system for long-term motion-tolerant wearable monitoring of blood pressure and heart rate with ear-ECG/PPG. *IEEE Access* **5**, 10547–10561 (2017).
34. Zhang, Q., Zhou, D., & Zeng, X. PulsePrint: single-arm-ECG biometric human identification using deep learning. *IEEE 8th Annual Ubiquitous Computing, Electronics and Mobile Communication Conference (UEMCON)* 452–456 (IEEE, 2017).
35. Abdeldayem, S. S. & Bourlai, T. A novel approach for ECG-based human identification using spectral correlation and deep learning. *IEEE Trans. Biom. Behav. Identity Sci.* **2**, 1–14 (2019).
36. Bao, X., Abdala, A. K. & Kamavuako, E. N. Estimation of the respiratory rate from localised ECG at different auscultation sites. *Sensors* **21**, 78 (2020).
37. Santurkar, S., Tsipras, D., Ilyas, A. & Mądry, A. How does batch normalization help optimization? in *Proc. 32nd International Conference on Neural Information Processing Systems* 2488–2498 (NeurIPS, 2018).
38. He, K., Zhang, X., Ren, S. & Sun, J. Delving deep into rectifiers: surpassing human-level performance on ImageNet classification. In *Proc. IEEE International Conference on Computer Vision* 1026–1034 (IEEE, 2015).
39. McInnes, L. et al. UMAP: uniform manifold approximation and projection. *J. Open Source Softw.* https://doi.org/10.21105/joss.00861 (2018).

Methods

Chemicals

Gold(III) chloride trihydrate, oleylamine, triisopropylsilane (99%), 4-mercaptobenzoic acid, (3-aminopropyl)triethoxysilane, sodium citrate tribasic dihydrate (99.0%), L-ascorbic acid, polymethyl methacrylate, hexane, liquid metal (Eutectic gallium-indium) and ethanol (analytical grade) were purchased from Sigma-Aldrich. Polymethyl methacrylate (PMMA; 950 A6) was purchased from MicroChem. A positive photoresist AZ 1512 and developer AZ 726 MIF were received from Microchemicals GmbH. The bare silicon wafer <100> was purchased from the Electronics and Materials Corporation. The PDMS elastomer base and curing agent (Sylgard 184) were received from Dow Corning. All solutions were prepared using Millipore Milli-Q water (resistivity > 18 MΩ cm^{-1}). All chemicals were used as received unless otherwise indicated. Conductive wires were purchased from Adafruit.

Synthesize of u-AuNWs

Ultrathin gold nanowires were synthesized as described in refs. 21,40. In detail, 44 mg gold(III) chloride trihydrate was added to 40 ml hexane solution; 1.5 ml oleylamine was then added, which led to the dissolution of the gold salts; and finally triisopropylsilane was added after the gold salts were fully dissolved. The as-prepared solution was left at ambient conditions for 24 h without stirring until the colour turned from yellow to dark red due to the formation of ultrathin AuNWs. The nanowires solution was collected by repeated centrifugation and thorough washing with ethanol/hexane (2/1, v/v); it was finally concentrated to a 2 ml stock solution in hexane for further use[21,40].

Fabrication of v-AuNWs/PDMS thin film

The v-AuNWs were fabricated on the basis of a modified seed-mediated approach[16]. First, 2 nm gold seeds were synthesized through mixing 0.25 ml 25×10^{-3} M gold(III) chloride trihydrate and 0.147 ml 3.4×10^{-2} M sodium citrate in a conical flask with 20 ml H_2O under vigorous stirring; 1 min later, 600 µl of ice-cold 0.1 M $NaBH_4$ solution was added to the solution, which was stirred for 5 min until the colour turned from light yellow to red. The gold seed solution was stored in the fridge at 4 °C until needed. To fabricate a patterned photomask for the growth of v-AuNWs, a thin PMMA layer was first spin-coated onto a bare silicon wafer at 3,000 r.p.m. for 45 s, followed by baking at 180 °C for 2 min. The photoresist was then spin-coated on top of PMMA layer at 3,000 r.p.m. for 45 s; v-AuNW patterns were formed via a conventional photolithography process. To grow v-AuNWs, the exposed PMMA surface was treated with oxygen plasma for 5 min. The silicon wafer was then immersed in a 5×10^{-3} M (3-aminopropyl)triethoxysilane ethanol solution for 2 h to functionalize the surface with an amino group. After twice rinsing with ethanol, the amino-functionalized surface was immersed into citrate-stabilized gold seed solution for 2 h, followed by rinsing with water twice to remove excess seed particles. Finally, the gold seed-modified substrates were immersed in a growth solution with 9.8×10^{-4} M 4-mercaptobenzoic acid, 1.2×10^{-2} M gold(III) chloride trihydrate and 2.9×10^{-2} M L-ascorbic acid for 1–5 min, leading to the formation of v-AuNWs thin films. After the growth of the v-AuNWs, the PDMS base and curing agent were mixed (w/w = 10:1, consistent throughout the paper unless otherwise indicated) and spin-coated on top of the v-AuNW thin film at 1,500 r.p.m. for 1 min. After curing at 80 °C for 3 h, the PDMS thin films were sectioned with a scalpel and peeled off from the substrate.

Fabrication of HR skin

First, HR layer 3 was fabricated by spin-coating the PDMS precursors onto a petri dish at 1,500 r.p.m. for 30 s, followed by curation at 60 °C for 2 h. The assembly of well-defined u-AuNW films was produced using a modified Langmuir–Blodgett technique[1]. The u-AuNWs thin films were prepared at ambient conditions in a 9 cm petri dish using Millipore Milli-Q water as a subphase. Due to the hydrophobic ligands of u-AuNWs, a self-assembled nanowire thin film can form and fully cover the water surface after dispersing the u-AuNW suspension onto the water subphase drop by drop[41]. After 3 min equilibration, u-AuNWs thin films can be transferred onto mask-defined PDMS substrates through horizontal deposition[21]. Furthermore, multilayer u-AuNW films (2–5 layers) could be realized by repeating the transfer method described above. Then, HR layer 2, with through holes at both ends, was bonded on top of HR layer 3 after 2 min oxygen plasma treatment. HR layer 1 was fabricated by spin-coating the PDMS precursors onto a petri dish at 1,500 r.p.m. for 30 s, followed by sputter coating a layer of platinum at 0.3 nm s^{-1} for up to 3.5 min. Parallel vertical cracks were generated on the platinum thin film by applying a tensile strain of 5% using a motorized moving stage (THORLABS Model LTS150/M). Both ends of HR layer 1 were punched with through holes and laminated onto HR layer 2 enhanced by plasma bonding. Finally, a thin PDMS layer (spin-coating at 1,500 r.p.m. for 30 s) was bonded on top as encapsulation after wiring the device with liquid metal and conductive copper wires.

Characteristics of the HR skin

Scanning electron miscroscope images were collected using a FEI Helios Nanolab 600 focused ion beam microscope (operating voltage of 5 kV and current of 86 pA). Transmission electron microscope images were characterized with a FEI Tecnai G2 F20 FEGTEM equipped with a Bruker 30 mm^2 123 eV windowless silicon drift detector. Optical images were taken by a Nikon ECLIPSE LV150 microscope with a Nikon Digital Sight DS-Fi1 camera. The sheet resistances measurement was taken with a Jandel four-point conductivity probe with a linear arrayed four-point head. To test the electro-strain responses of the HR skin and individual layers, both ends of the samples were attached to a motorized moving stage (THORLABS Model LTS150/M). Stretching cycles with a constant speed were controlled by a computer-based user interface (Thorlabs APT user), whereas the current/voltage/resistance changes were measured by a VERSASTAT 3–500 electrochemical system (Princeton Applied Research). The acoustic sensing was characterized by playing a piece of sound with a constant frequency between 80–1,000 Hz using a loudspeaker under the sensors at 1–5 mm distance. A Compact Digital Sound Level Meter (Jaycar, QM1589) was fixed near the sensors to measure the sound pressure level around the device. To test the electro-pressure responses, the samples are suspended on a test stand (Mark-10, ESM 301L) while a motorized probe with a force gauge (Mark-10 series 7–20) was approaching on top to provide a pressure. The speed and force were controlled by a Mark-10 MESURgauge Plus software. The plasma treatment was conducted in a Harrick plasma cleaner at a pressure of 500 Pa.

Data collection

Heart and respiration rates: three participants (male 1, 34 years old; female 1, 33 years old; male 2, 30 years old) were tested with different heart and respiration rates of 60–80 beats per minute and 12–20 breaths per minute, respectively. The data are split into 1 min segments and then passed through different bandpass filters for relevant rate detection. A MightySat Rx Fingertip Pulse Oximeter was used as a reference device to monitor real heart rate and breath rate.

Eleven classes of throat activities: one male participant (male 1, 34 years old) and one female participant (female 1, 33 years old) were recruited to collect speech, breathing, pulse, movement and press activity. In each experiment, participants were instructed to sit comfortably on the chair while attaching the HR skin onto their throat. The time-series signals were collected by a VERSASTAT 3–500 electrochemical system (Princeton Applied Research). All of the samples in each class were collected >100 times, with a duration of 5 s. The overall dataset contains 11 classes of activities with 2,011 data samples.

Validation of DeepHS model with different subjects: five participants (male 1, 34 years old; male 2, 30 years old; male 3, 27 years old; female 1, 33 years old; female 2, 30 years old) were recruited to

collect speech, breathing, pulse, movement and press activity. All of the samples in each class were collected >10 times, with a duration of 5 s. Informed consent was obtained from the participants, all of whom were volunteers.

Data processing

We employed common data preprocessing techniques before passing the final signal to the neural network. In the training process, initially, as each data file we collected contained multiple samples from each person and based on the characteristics of sample signals, we developed a segmentation tactic that guaranteed not only all samples have the same length (3,000 points in 3 s), but also the peak of the current signal in each sample was at around 1,500 points, meaning about 1.5 s. Then we obtained the frequency response using the STFT algorithm over each sample. Particularly worth mentioning was that the original samples were one-dimension signals, and the STFT samples were two-dimension phase-dropped spectrograms. Due to the fixed window function, window size and related padding methods, the resolutions of the STFT are determined as 257 for the frequency domain and ten for the time domain.

Visualization

The virtual environment was developed using Unity3D and can be shared on reasonable request.

Data availability

All relevant data are available from the authors on reasonable request, and/or are included within the manuscript and its Supplementary Information. The machine learning datasets used in this study are available at https://github.com/XinZ0419/Deep-Hybrid-Spectro. Source Data are provided with this paper.

Code availability

The code that supports the plots within this paper and other findings of this study are available at https://github.com/XinZ0419/Deep-Hybrid-Spectro.

References

40. Gong, S. et al. Fabrication of highly transparent and flexible nanomesh electrode via self-assembly of ultrathin gold nanowires. *Adv. Electron. Mater.* **2**, 1600121 (2016).

41. Chen, Y., Ouyang, Z., Gu, M. & Cheng, W. Mechanically strong, optically transparent, giant metal superlattice nanomembranes from ultrathin gold nanowires. *Adv. Mater.* **25**, 80–85 (2013).

Acknowledgements

This research was financially supported under Discovery Projects funding scheme (grant nos. DP180101715, DP200100624 and DP210101045) and Jack Brockhoff foundation (JBF grant no. 4659-2019). This work was performed in part at the Melbourne Centre for Nanofabrication (MCN) in the Victorian Node of the Australian National Fabrication Facility (ANFF). The authors also acknowledge the use of facilities at the Monash Centre for Electron Microscopy.

Author contributions

S.G. and W.C. conceived the idea, designed the experiment, and composed the manuscript. W.C. and Z.G. supervised the whole project. S.G., X.Z., X.A.N., Q.S. and F.L. performed all of the experiments. All authors made technical comments on the manuscript. W.C. submitted the manuscript and was the lead contact.

Competing interests

W.C. declares that the v-AuNW growth on PDMS is related to the patented technology (patent nos. US11387012B2 and AU2018263276B2) that has been licensed to Soft Sense Pty Ltd in which W.C. is the founder. The other authors declare no competing interests.

Additional information

Supplementary information The online version contains supplementary material available at https://doi.org/10.1038/s41565-023-01383-6.

Correspondence and requests for materials should be addressed to Zongyuan Ge or Wenlong Cheng.

Peer review information *Nature Nanotechnology* thanks Bin Ding and the other, anonymous, reviewer(s) for their contribution to the peer review of this work.